Finely Iron-Dispersed Particles on Beta Zeolite from Solvated Iron Atoms: Promising Catalysts of NH_3-SCO

S. Campisi,[§] S. Palliggiano,[§] A. Gervasini[*,§,≠] and C. Evangelisti,[*,≠]

[§] Dipartimento di Chimica, Università degli Studi di Milano, via Camillo Golgi 19, I-20133 Milano, Italy

[≠] CNR - ISTM - Istituto di Scienze e Tecnologie Molecolari, Via G. Fantoli 16/15, 20138 Milano, Italy

ABSTRACT

Beta zeolite has been functionalized with ca. 2 wt.% Fe to obtain catalysts for the NH_3-SCO reaction. Iron deposition was performed on the zeolite surface by solvated metal atom dispersion (SMAD) and ionic-exchange (IE) procedures. ZSM-5 was selected as reference structure known to assure high dispersion of isolated centers when functionalized with iron by IE. Transmission electron microscopy techniques combined with element maps enlightened on the iron-species distribution and dimension on the two zeolites. As expected, highly homogeneous dispersed iron species were present on the ZSM-5 sample prepared by IE, while with Beta zeolite the same deposition method led to the formation of FeO_x aggregates (2.5-10 nm) together with isolated iron species. On the other hands, by SMAD approach, well-formed FeO_x-nanoparticles ranging 1.0 – 4.5 nm were revealed on Beta zeolite.

Ammonia oxidation activity (NH_3-SCO) on iron-containing zeolites started at ca. 300°C, without no clear effect of the size of Fe on the reaction activity/selectivity. Ammonia conversion regularly increased with temperature with always very high selectivity to dinitrogen (98-100%), without any NO_x or N_2O formation, on iron containing Beta zeolites, in particular. Only very limited increase of iron particle dimensions were observed on the used Fe-catalysts, in any case.

The collected experimental results indicated that not only isolated well-dispersed iron species are associated with high activity and selectivity in the NH_3-SCO reaction. SMAD-derived iron nanoparticles worked with excellent performances in the ammonia oxidation reaction with high activity in terms of conversion, selectivity to dinitrogen, and stability.

Keywords: zeolites; dispersed iron phase; solvated metal atom dispersion; ionic exchange; selective catalytic oxidation of ammonia.

1. INTRODUCTION

Ammonia is one of the major building blocks of the chemical industry today, being involved in the processing of a great number of manufactured products. According to recent estimates, about 44-55 million tons per year of gaseous ammonia are released into the atmosphere and 75-95% of emissions derive from agriculture activities (livestock, fertilizer, etc.).[1-3] Hypertrophication, acidification, and formation of atmospheric particulate matter ($PM_{2.5}$) are among the main consequences of NH_3 release in the atmosphere.[4,5] Although the adoption of common prevention and control strategies caused the ammonia emissions to fall by 25% in Europe between the years 1990 and 2011,[6] as a general trend, emissions are destined to rise on a global scale in the next decades.[1-3] The expected increase in NH_3 emissions is related to the growing contribution of non-agricultural sources including bio- and fossil fuel combustion, industrial processes involving ammonia as reactant or by-product, and emission abatement technologies (i.e. diesel exhaust fluid DEF, DeNOx technologies).[7] In particular, the need to accomplish ever stricter emission standards for NO_x results in the use of an excess of NH_3 in the selective catalytic reduction (NH_3-SCR) for improving the efficiency of the NOx abatement.[8] However, this solution entails the risk of the so called "ammonia slip" referring to the emission of unconverted ammonia, which constitutes a not negligible issue of scientific concern.

Among the current strategies for ammonia emission control,[9] including scrubbing, adsorption, liquefaction, biofiltration, catalytic combustion, catalytic decomposition, thermal and selective catalytic oxidation, the latter represents the most suitable method for the treatment of oxygen-rich ammonia slipstream.[10] In the ammonia selective catalytic oxidation (NH_3-SCO), NH_3 is selectively oxidized to molecular nitrogen and water vapour according to (Eq.1) in the presence of a proper catalyst aimed at minimizing the occurrence of side-reactions, (Eq.2) and (Eq.3), which would result in the formation of harmful nitrogen oxides.

$$4NH_3 + 3O_2 \rightarrow 2N_2 + 6H_2O \qquad \text{(Eq.1)}$$

$$4NH_3 + 5O_2 \rightarrow 4NO + 6H_2O \qquad \text{(Eq.2)}$$

$$2NH_3 + 2O_2 \rightarrow N_2O + 3H_2O \qquad \text{(Eq.3)}$$

Depending on the catalyst nature, reaction conditions and oxygen availability, the NH_3-SCO reaction can proceed according to different mechanisms: the imide nitrosyl mechanism, the hydrazine mechanism and the *internal SCR mechanism*.[10-13] All the proposed mechanisms involve the interaction of ammonia with acid sites. However, understanding the mechanism and its relation with the active site structure is fundamental for the optimization of NH_3-SCO catalysts which optimization for real application remains an open challenge.

The ideal catalyst should be selective and active in a broad temperature range and should possess high water-tolerance and very low sensitivity to sulphur poisoning.[14,15] In the last decades, several catalytic systems have been proposed for this process, such as supported or unsupported noble metals,[16-18] transition metal oxides,[16,19-21] and mixed oxides.[22-25] In particular, iron[26-28] and copper[28-31] oxides have demonstrated to be active and selective catalysts. On the other hand, Fe and Cu resulted to be active and selective species also when encapsulated as ions inside zeolitic frameworks,[31-33] probably due to the possibility to work in two different oxidation states (Fe^{2+}/Fe^{3+} and Cu^{2+}/Cu^{+}).[33]

Concerning zeolites, most of the articles appeared in the literature have been devoted to unravel the effect of the zeolitic support morphology,[34,35] aluminium content,[36] copper/iron precursor,[37], deposition method[33] on the catalytic performances. Extensive investigations have been done on the effect of the topology of zeolitic framework in the NH_3-SCO process and excellent reviews report comparative information on a large number of zeolite structures functionalized with copper and iron, in particular.[10,31] Specifically, iron-modified ZSM-5 zeolite (Fe/ZSM-5) revealed to be the most NH_3-SCO promising catalyst. Less attention has been devoted to the effect of the deposition method of the metallic species that can accommodate on the zeolite surface as isolated species or in more aggregated form with expected consequences on the catalytic behaviour. Akah et al.[33] compared the oxidation performances of Fe/ZSM-5 catalysts prepared by impregnation, ion exchange, and hydrothermal synthesis. Good activity (NH_3 conversion between 60-70% at 400°C) and high selectivity to N_2 (95-100%) were obtained when iron was added in *post-synthesis* on zeolite structure by wetness impregnation and ion-exchange technique.

In this work, for the first time we report the deposition of iron phase on Beta zeolite by the solvated metal atom dispersion method (SMAD).[38-40] This approach provides a valuable synthetic route to weakly stabilized noble (e.g. Pd, Pt, Au)[41-43] and *non*-noble (e.g. Cu),[44,45] metal nanoparticles, named solvated metal atoms, which can be easily immobilized onto different kind of supports guarantying a high dispersion of the metal phase. In order to unravel interesting relation between aggregation state of the metal phase and the corresponding catalytic performances, low concentration (ca. 2 wt.%) of iron has been deposited either by SMAD or classical ionic-exchange method (IE).

The selected Beta zeolite structure, which is less studied compared to the conventional ZSM-5 structure, has a very complex structure; it consists of an intergrowth of two distinct structures termed polymorphs A and B. The polymorphs grow as two-dimensional sheets and the sheets randomly alternate between the two. Both polymorphs have a three dimensional network of 12-ring pores. The intergrowth of the polymorphs does not significantly affect the pores in two of the dimensions, but in the direction of the faulting, the pore becomes tortuous, but not blocked.[46] The comparison between Fe-catalysts prepared by ionic exchange on Beta and ZSM-5 zeolites and between two different methods of Fe-deposition on Beta zeolite allowed to investigate the effect of zeolite framework topology and of the deposition method, respectively, on the activity and selectivity of the NH_3-SCO reaction.

2. MATERIALS AND METHODS

2.1. Materials

Fe-containing catalysts have been prepared from commercial zeolite samples: NH_4-ZSM-5 (from Süd-Chemie, NH_4-MFI 27, with SiO_2/Al_2O_3 molar ratio of 28) and Beta-zeolite (from Süd-Chemie, H-BEA 25, with SiO_2/Al_2O_3 molar ratio of 30).

Iron nitrate $Fe(NO_3)_3 \cdot 9H_2O$ from Sigma-Aldrich (> 99.95% purity grade) was used as iron precursor for IE method. Iron Chips (99.98 %) were from Aldrich. Acetone was distilled under argon. The co-condensation of iron and acetone vapors was carried out in a static metal vapor synthesis (MVS) reactor already described.[39,40] An amorphous iron containing silica-alumina (5 wt.% Al_2O_3 and SiO_2/Al_2O_3 molar ratio of 30) sample has been used as reference material (here below labelled Fe/SA, with 5.9 wt.% Fe). Preparation and main structural and morphological features are reported in Ref.47. Gas mixtures (NH_3/He 2.08%mol, O_2/N_2 20.08%) for NH_3-SCO catalytic tests were purchased from SAPIO, Italy.

2.2. Catalyst Preparation

Zeolitic samples have been functionalized with low amount of Fe by two different methods: ionic exchange (I.E.) and solvated metal atom dispersion (SMAD).

According to I.E. procedure, starting from NH_4-ZSM5 and Beta zeolite samples, aqueous iron nitrate solutions ($Fe(NO_3)_3 \cdot 9H_2O$), with defined volume and concentration to give rise to a $mol_{Fe}/m_{zeolite}$ ratio equal to ca. 0.4, have been contacted with the zeolite powders at 40°C for 24h under stirring. After centrifugation, thoroughly washing with hot water (40°C), drying at 110°C overnight, final samples have been recovered (Fe/ZSM-5_{IE} and Fe/$Beta_{IE}$).

According to SMAD procedure starting from Beta zeolite sample, in a typical experiment, Fe vapors generated by resistive heating of an alumina-coated tungsten crucible, filled with ca. 500 mg of iron, were co-condensed at -196°C with acetone (100 mL) in the glass reactor chamber for 1 hour. The reactor chamber was then warmed to the melting point of the solid matrix (ca. -95°C), and the resulting brown solution (95 mL) was siphoned at a low temperature into a Schlenk tube and kept in a refrigerator at -20°C. The Fe-content of the Fe-solvated metal atoms (SMA) solution were 0.55 mg mL^{-1}, as determined by ICP-OES analysis. Fe NPs were then quantitatively supported onto Beta zeolite by adding 91 mL of the Fe-SMA solution to a suspension of the zeolite (2.5 g) in acetone (50 mL) under stirring at 25°C for 20 h. The colorless supernatant acetone was then removed. The Beta zeolite-supported Fe NPs (Fe/Beta$_{SMAD}$) were dried under vacuum (10^{-3} mBar) and treated in a static air muffle oven at 120°C overnight. The isolated catalyst contained 2.0 wt. % of Fe, as confirmed by ICP-OES analysis.

2.3. Catalyst Characterization

Iron concentration was evaluated by Uv-vis Spectrophotometry for ionic-exchange prepared catalysts and by Ion Coupled Plasma Optical Emission Spectroscopy (ICP-OES) for SMAD prepared samples. UV-vis spectra on iron solution were collected at 470 nm on Beckman Coulter DU640 Spectrophotometer according to thiocyanate method. ICP-OES analyses of the supported catalysts were carried out with an iCAP 6200 Duo upgrade, Thermofisher instrument with external calibration for Fe content. In a typical experiment, a sample (5.0 mg) of the catalyst was heated over a heating plate in a porcelain crucible in the presence of *aqua regia* (2.0 mL) for four times, and then treated with 0.5 M aqueous HCl and filtered on PTFE 0.2µm filters. The limit of detection (lod) calculated for iron was 5 ppb.

The nitrogen (99.9995% purity) adsorption/desorption isotherms were collected at -196°C using a SA™ 3100 version instrument from Beckman Coulter. Prior to the analysis, the samples were outgassed at 200°C for 1 h under vacuum. The surface area was calculated using the BET equation (N_2 molecular area of 16.2 Å^2). *t-Plot* method (by using the reference Harkins-Jura isotherm) allowed measuring the external surfaces as well as the microporosity.

Routine powder X-ray diffraction patterns were recorded at room temperature (RT) using a Philips Powder X-ray diffractometer equipped with a PW 1830 generator, monochromator in graphite, with Cu Kα ($\lambda = 1.5418$Å) radiation. The X-ray tube operated at 40 kV × 40 mA. The diffraction patterns were collected in the 5°–60° 2θ range.

X-ray photoelectron Spectroscopy (XPS) analysis were carried out on a M-PROBE Surface Spectrometer, using an Al (Kα) source and a spot size from 0.15 mm to 1 mm in diameter. The voltage was 10V and the vacuum 10^{-8} Torr. The survey scans were carried out in the binding energy range 0-

1000 eV, using a spot size of 800 micron. The software used for data analysis was ESCA Hawk Software.

Transmission electron microscopy (TEM) analysis on iron-based catalysts were performed using a ZEISS LIBRA200FE microscope equipped with a 200 kV FEG source. Energy-dispersive X-ray spectra (EDS – Oxford INCA Energy TEM 200) and elemental maps were collected along with HAADF-STEM (high angular annular dark field scanning transmission electron microscopy) micrographs. The samples were finely smashed in an agate mortar, suspended in isopropanol and sonicated, then each suspension was dropped onto a lacey carbon-coated copper grid (300 mesh) and the solvent was evaporated. The histograms of the metal particle size distribution for the samples were obtained by counting at least 500 particles onto the TEM micrographs. The mean particle diameter (d_m) was calculated by using the formula:

$$d_m = \sum d_i n_i / \sum n_i \qquad \text{(Eq.4)}$$

where n_i is the number of particles with diameter d_i.

Diffuse reflectance spectra (DRS) of the Fe-samples were measured on a double beam UV–vis–NIR scanning spectrophotometer (Shimadzu UV-3600 plus, Japan) equipped with a diffuse reflectance accessory (integrating sphere from BIS-603). A given amount of the powder sample, finely grinded, was uniformly pressed in a circular disk (E.D., *ca*. 1 cm) included in the sample-holder; the latter was inserted in a special quartz cuvette and then put on a window of the integrating sphere for the reflectance measurements. The measured reflectance spectra ($R\infty$,%) were converted to absorbance (Abs) using Eq. 5:

$$\text{Abs} = \text{Log}\,(1/R\infty/100) \qquad \text{(Eq.5)}$$

Acidity of the samples was evaluated by NH_3 probe adsorption in flowing dynamic experiments. The dried and weighted sample, put on a porous septum in a quartz reactor, was activated at 120°C under flowing air for 30 min. Then, it was maintained at the same temperature of 120°C while a NH_3/He mixture, with NH_3 concentration of ca. 500 ppm, flowed at 6 NL h^{-1} through it and entered in a gas cell (path length 2.4 m multiple reflection gas cell) in the beam of an FTIR spectrometer (Bio-Rad with DTGS detector). On each sample, NH_3 was completely adsorbed for a given measured time, as observed from the trace of the NH_3 line at 966 cm^{-1}, that was recorded as a function of time. When the saturation of the acid sites under the flowing NH_3 concentration was attained, the NH_3 signal was restored at level corresponding to its concentration in the starting mixture. From the evaluation of the time during which the NH_3-signal has remained to zero, the amount of acid sites has been evaluated, as follows:

$$\frac{moles_{NH_{3(ads)}}}{g_{sample}} = \frac{[NH_3]_{fed} \cdot F \cdot t \cdot P}{RT \cdot m_{sample}} \qquad \text{(Eq.6)}$$

where $[NH_3]_{fed}$ is the flowing NH_3 concentration, in ppm; F is the total flow rate of the NH_3/He mixture, in $NL \cdot h^{-1}$; t is the time during which NH_3 was completely adsorbed, in min; P is the pressure, in atm; and m_{sample} is the mass of the sample, in g.

Assuming a 1:1 stoichiometry for the NH_3 adsorption on the surface acid site, the amount of acid sites *per* sample mass or *per* surface unit (in $\mu equiv \cdot g^{-1}$ or $\mu equiv \cdot m^{-2}$) was evaluated.

Temperature programmed reduction (H_2-TPR) experiments were carried out on the Fe-containing samples using a Micromeritics Pulse Chemisorb 2700 instrument. The samples (*ca.* 0.08 g) were initially pre-treated in air flow at 350°C for 1 h. After cooling to 50°C, the H_2/Ar (5.03% v/v) reducing mixture flowed at 20 mL min^{-1} through the sample whose temperature increased from 50 to 900°C (8°C min^{-1}). The H_2 consumption was detected by a thermal conductivity detector (TCD). Peak areas were calibrated with pure H_2 injections (Sapio, Italy; 6.0 purity)

2.4. Catalytic Tests: NH_3-SCO

Before NH_3-SCO catalytic activity tests, all the catalyst samples were pressed, crushed and sieved to 45–60 mesh (catalyst particle size of 0.25–0.35 nm). Catalyst pre-treatment was performed in situ under O_2/He (20% v/v) atmosphere at 150°C for 60 min.

Reaction tests of NH_3 oxidation (NH_3-SCO) were performed in a fixed-bed glass tubular microreactor (5 mm ID) put in a tubular vertical electric oven (maximum temperature 1000°C). The catalytic tests were carried out at atmospheric pressure, at fixed space velocity, GHSV of ca. 50,000 h^{-1} and variable temperature in the interval of 150–450°C (Eurotherm Controller-Programmer type 818). Temperature was regularly increased with a rate of $5°C \cdot min^{-1}$. Each plateau of temperature was maintained for at least 60 min to allow the attainment of the steady-state conditions. Each catalytic run was repeated four times in selected intervals of temperature to check reproducibility of the measured activity and selectivity.

The mass of catalyst into the reactor was ca. 0.10 g with a total flow of the gaseous mixture at 6 NL h^{-1}. A set of mass flow controllers (Bronkhorst, Hi-Tec and Brooks Instruments) provided the accurate concentration of the reactant mixture: ca. 650 ppm NH_3 and 50,000 ppm of O_2 in helium.

The effluent gas mixtures from the reactor flowed through a gas cell (path length 2.4 m multiple reflection gas cell) in the beam of an FT-IR spectrometer (Bio-Rad with DTGS detector) where it was continuously analysed. The spectrometer response permitted the quantification of NO (at 1876 cm^{-1}), NO_2 (at 1619 cm^{-1}), N_2O (at 2236 cm^{-1}) and NH_3 (at 966 cm^{-1}). The measurements were carried out each 180 s with accumulation of 90 scans per spectrum and 2 cm^{-1} of resolution. During the catalytic tests, the total absorbance of all the IR active species (*Gram-Schmidt*) flowing from the reactor was monitored each 180 s. The concentration profile of each species detected as a function of time/temperature of reaction was determined on the basis of its typical wavelength, once known the molar extinction coefficient (determined by calibration experiments) from the decomposition of the *Gram-Schmidt* plot.

Conversion of NH_3 was calculated from the following formula, where $[NH_3]_{in}$ is the concentration of ammonia at 150°C and $[NH_3]_{out}$ is the concentration of ammonia (evaluated at steady state condition) at each reaction temperature:

$$NH_3\ conversion\ (\%) = \left(1 - \frac{[NH_3]_{out}}{[NH_3]_{in}}\right) \cdot 100 \qquad \text{(Eq.7)}$$

Selectivity to N_2, N_2O, NO_2, and NO can be computed from the following equations:

$$N_2 selectivity\ (\%) = \left(\frac{2[N_2]}{[NH_3]_{in} - [NH_3]_{out}}\right) \cdot 100 \qquad \text{(Eq.8)}$$

$$N_2O\ selectivity\ (\%) = \left(\frac{2[N_2O]}{[NH_3]_{in} - [NH_3]_{out}}\right) \cdot 100 \qquad \text{(Eq.9)}$$

$$NO\ selectivity\ (\%) = \left(\frac{[NO]}{[NH_3]_{in} - [NH_3]_{out}}\right) \cdot 100 \qquad \text{(Eq.10)}$$

$$NO_2\ selectivity\ (\%) = \left(\frac{[NO_2]}{[NH_3]_{in} - [NH_3]_{out}}\right) \cdot 100 \qquad \text{(Eq.11)}$$

$$NO_x\ selectivity\ (\%) = NO\ selectivity (\%) + NO_2\ selectivity (\%) \quad \text{(Eq.12)}$$

The calculation for the specific activity (Eq.13) was computed taking into account contact time (θ), expressed in g_{cat}·min·$mmol_{gas}^{-1}$:

$$Specific\ activity\ (mmol_{NH3} \cdot min^{-1} \cdot g_{cat}^{-1}) = \frac{[NH_3]_{in} - [NH_3]_{out}}{\theta} \qquad \text{(Eq.14)}$$

3. RESULTS

3.1. Catalyst Preparation and Characterization

Beta and ZSM-5 zeolites have been selected as frameworks for the deposition of iron phase by conventional ion-exchange procedure. The main properties of the two bare zeolite samples are listed in Table 1. They are both high-surface area materials with presence of microporosity, in particular H-ZSM-5 (Fig. 1). Addition of the iron phase resulted in a decrease of surface area and, in particular, of internal surface area for Fe/ZSM-5. This could be ascribed to a partial occlusion of the ZSM-5 micropores, as confirmed by the high reduction of micropore volume. Conversely, a sensitive increase of surface area as well as of micropore volume was observed in Beta after the addition of iron phase. On this structure, it can be guessed that larger Fe-aggregates were formed.

Size-controlled Fe nanoparticles supported on Beta zeolite were synthesized by SMAD method. The controlled co-condensation of Fe vapors and acetone vapors afforded mainly spherical Fe nanoparticles with a mean diameter 2.7 nm weakly stabilized by acetone, named Fe SMA[48]. The acetone solution containing Fe SMA was conveniently used to deposit highly dispersed FeO_x nanoparticles on Beta zeolite by simple impregnation of the support at 25°C avoiding the presence of stabilizing agents or byproducts deriving from the reduction step. This procedure did not significantly affect the morphological properties of the zeolite, which maintained similar surface area and porosity.

The morphological and structural properties of the different Fe-zeolite catalysts were investigated by HRTEM and HAADF-STEM microscopy combined with EDX analysis. Fe/ZSM5$_{IE}$ catalysts showed zeolite microcrystals (0.3-3 μm) with a defined shape (Fig. 2). HAADF-STEM/EDX element map on a ZSM5-based grain revealed, along the presence of silicon and aluminum atoms of the zeolite support, a highly homogeneous dispersion of iron atoms, thus suggesting that the loaded Fe was adsorbed within the pores, as expected from the IE procedure. Moving to the Beta zeolite-supported catalysts (Fig. 3), Fe/BETA$_{IE}$ showed zeolite grains being in the range 1-5 μm together with the presence of segregated iron aggregates (as confirmed by EDX analysis) mainly ranging 2.5-10 nm (mean diameter, d_m, = 5.9 nm, Table 2). This evidence could justify the observed increase in surface area and micropore volume. Although this segregation was unexpected for the IE procedure, this might be due likely to the presence of iron oxide clusters in the IE solution, whose acidity was limited in order to prevent the leaching of Al from the zeolite support. The acidic surface of the support might have then anchored the Fe oxide clusters, creating the nanoparticles. On the other hand, the deposition of Fe nanoparticles by SMAD procedure (Fig. 4) led to the formation of small metal particle size (d_m = 2.5 nm) with a narrower size distribution (1.0 - 4.5 nm) when compared to the sample prepared by IE (Tab. 3).

All the samples exhibited a vivid colour, ranging from light yellow for Fe/ZSM-5$_{IE}$ to brown for Fe/SA. The different colours were symptomatic of a different coordination of iron centres in the iron containing materials. Iron coordination environment can be identified by Ultraviolet-visible diffuse reflectance spectroscopy (UV-vis DRS), which allowed to investigate iron speciation on zeolite surfaces. UV-vis DR spectra were recorded in the range between 200 and 2000 nm on the four samples and they are shown in Fig. 5 limited to the 200-800 nm region. Indeed, characteristic absorption signals of iron species are observed in this range and they can be ascribed either to *d-d* (ligand field) transitions or to ligand to-metal charge-transfer (CT) excitations from the O(2p) non-bonding valence bands to the Fe(3d) ligand field orbitals. The occurrence and the exact position of the absorption bands can provide useful information on the iron speciation.[49] However, overlapping between different signals usually resulted in the appearance of complex bands, thus deconvolution in sub-bands was necessary to identify the different contributions. All the spectra presented two contributions below 300 nm which can be caused by CT transitions in isolated iron centres. In particular, tetrahedrally coordinated Fe^{3+} ions give rise to absorptions in the region between 190 and 240 nm, while bands in the 250-280 nm are associated with isolated Fe^{3+} ions in a higher (typically octahedral) coordination.[49,50] However, CT transitions are not exclusively ascribable to isolated iron centres. Indeed, such transitions are expected, too, for Fe^{3+} in more aggregated states (Fe-O-Fe oligomers or Fe_xO_y nanoparticles).[51] Differently, the presence of d-d transition bands is usually associated uniquely with the presence of iron oligomers (300-350 nm) and iron oxide nanoparticles (450-550 nm). In fact, d-d transitions from the ground state ($^6A_1$) to excited ligand field states ($^4T_1$, $^4T_2$, ^4E) are spin forbidden and therefore they would be characterised by weak intensity; however, they become more intense when magnetic coupling occurs between neighbour iron centres in the aggregated systems.[49] Interestingly these bands are absent or less intense in the case of Fe/ZSM-5_{IE}, confirming the limited aggregation and high dispersion of isolated iron centres on ZSM-5 surface. On the contrary, Fe_xO_y nanoparticles and iron oligomers are predominant species in Fe/$Beta_{SMAD}$ and Fe/SA. Table S1 lists the band attributions of the deconvoluted curves.

The addition of iron centers on the zeolite surfaces could affect the surface acidity as a function of the iron dispersion and speciation: the more dispersed and accessible the iron phase, the higher is the number of acid sites. Solid-gas acid-base titrations were, then, performed using ammonia as base probe molecule to evaluate the acidity of Fe/zeolite samples. Higher amount of acid sites (1065 μequiv g^{-1}) was detected in Fe/ZSM-5_{IE}, as expected from the high iron dispersion observed by HAADF-STEM/EDX. Concerning Fe-loaded Beta zeolites, the acid site density was higher for Fe/$Beta_{IE}$ (952 μequiv g^{-1}) than for Fe/$Beta_{SMAD}$ (486 μequiv g^{-1}). This trend could appear in contrast to the evidences from transmission electron microscopy analysis, where larger aggregates were detected on Fe/$Beta_{IE}$ compared to Fe/$Beta_{SMAD}$. However, it can be guessed that ion exchange procedure results in the co-occurrence of isolated iron centers besides detectable large iron aggregates on Fe/$Beta_{IE}$.

The differences in the aggregation of iron phases unavoidably reflected also on the iron availability at the surface. In fact, XPS analysis unveiled remarkable discrepancies in terms of surface iron concentration between Fe/ZSM-5_{IE}, Fe/$Beta_{IE}$ and Fe/$Beta_{SMAD}$, while the total iron loading being similar. Only a very low amount of iron (0.47 atom%) was exposed at the surface of Fe/ZSM-5_{IE}, likely due to the migration of iron ions inside the micropores of ZSM-5 framework. An intermediate situation was observed in Fe/$Beta_{IE}$ (0.74 atom%), where large iron aggregates are probably concentrated at the surface, while isolated iron centers, probed by NH_3, are preferentially located inside the pores, thus are accessible to NH_3 but they cannot be probed by XPS. Finally, a high iron surface concentration characterizes Fe/$Beta_{SMAD}$ samples, coherently with the presence of very small iron nanoparticles.

Definitively, from the combination of the used characterization techniques, it emerges that the zeolite topology as well as the deposition procedure strongly influenced the nuclearity of iron phase on zeolite (Scheme 1). In particular, isolated iron centers are introduced on ZSM-5 by IE method. The latter gives rise to the co-presence of larger aggregates and isolated iron centers on Beta. Conversely, when SMAD approach was used to deposit the iron phase on Beta, small nanoparticles are homogeneously dispersed on the zeolite surface.

3.2. Catalytic Results

The catalytic performances of Fe-zeolite catalysts were evaluated in the NH_3-SCO reaction in the temperature range between 150°C and 450°C, at fixed GHSV of 50,000 h^{-1} and initial NH_3 concentration of 650 ppm. For each catalyst, different runs have been performed to check the catalyst stability.

The catalytic results are shown in Fig.s 6 and 7, depicting NH_3, N_2 and N_2O concentration profiles as a function of the temperature for the catalysts prepared by ion-exchange and SMAD method, respectively. For comparison the catalytic behavior of Fe_2O_3 nanoparticles (Table 2) deposited on silica alumina (Fe/SA) was also studied (Fig. 8).

All the studied catalysts were active in the 300-450°C temperature range and N_2 was the main product, although interesting differences emerged among the catalysts depending on the zeolite topology and the preparation methods. In particular, comparing catalysts prepared by IE procedure, it seems that the zeolite topology can influence the catalytic activity. Indeed, in the case of $Fe/Beta_{IE}$ NH_3 concentration curve started to decline at 300°C and NH_3 was quantitatively converted above 400°C, while over Fe/ZSM-5_{IE} catalyst NH_3 conversion started at slightly higher temperature (325°C) and was complete above 450°C. This difference could be ascribed to the different iron nuclearity and dispersion on the two catalysts, as demonstrated by transmission electron microscopy techniques and NH_3 adsorption experiments. The key role of the support appear more evident when Fe/SA is considered. Actually, Fe/SA catalyst was able to completely convert NH_3 in a quite similar temperature range (325-425°C, Fig. 8) than Fe/ZSM-5_{IE} and $Fe/Beta_{IE}$, however a different product distribution was observed. Indeed, differently from Fe/ZSM-5_{IE} and $Fe/Beta_{IE}$, in the case of Fe/SA the amount of produced N_2 remarkably decreased above 400°C, with formation of N_2O from the unselective NH_3 overoxidation. The concentration profiles of N_2 on $Fe/Beta_{SMAD}$ were not so dissimilar than the ones obtained on $Fe/Beta_{IE}$.

It is worth noting that for each catalyst a close overlap between concentration profiles from different runs was observed, thus suggesting a significant stability of the catalysts.

Useful structure-activity relations can be deduced from the quantitative catalytic and kinetic results reported in Table 3. From specific activity data, the following order can be deduced: Fe/Beta$_{SMAD}$ > Fe/Beta$_{IE}$ ≈ Fe/SA >> Fe/ZSM-5$_{IE}$. This activity trend is also evidenced in Fig. 9, where ammonia conversion curves are plotted as a function of the temperature. The curve corresponding to Fe/ZSM-5$_{IE}$ catalysts is clearly separated and shifted at higher temperature than the other curves. This evidence corroborates the hypothesis that isolated iron species are less active than iron aggregates in agreement with the literature.[52,53]

Fe/Beta$_{SMAD}$ emerged as the best catalyst in terms of both activity (4900 μmol g^{-1} min^{-1}) and selectivity to N_2 (>99% at 90% conversion). The excellent performances exhibited by Fe/Beta$_{SMAD}$ could be associated with the small iron particle size (*ca*. 2.5 nm).

In any case, good results were obtained also when larger nanoparticles (*ca*. 6 nm) are deposited on Beta zeolite by IE. This implies that not only the iron phase aggregation but also the zeolite topology plays a key role. Indeed, Fe/SA catalyst was less active and selective than Fe/Beta$_{IE}$ despite the similar mean iron particle sizes.

From a kinetic point of view, the NH_3-SCO could be considered as a first order reaction for all the catalysts, since an excess concentration of O_2 (50,000 ppm) was used. By monitoring, at a fixed contact time for each catalyst, the changes in NH_3 concentration as a function of the temperature, it was possible to calculate the reaction kinetic constant at each investigated temperature (k_T). Subsequently, from Arrhenius-type plots the activation parameters (apparent activation energy and pre-exponential factor A) have been computed (Table 3). The apparent activation energy values of the reaction on the Fe/ZSM-5$_{IE}$ and the Fe/Beta$_{IE}$ catalysts were quite equal (ca. 100 kJ mol^{-1}) and lower than the ones computed for Fe/Beta$_{SMAD}$ and Fe/SA (140 and 133 kJ mol^{-1}, respectively). A similar trend was found for the pre-exponential factor. These results provide further evidence that the reaction proceeds with different pathway on the studied catalysts. In particular, isolated iron centres present lower activation energy but are less active at high temperature than small iron aggregates.

It can be guessed that the catalytic behavior of the Fe-zeolite samples in the ammonia oxidation reaction is directly related to the different reducibility of the iron species depending on their aggregation state and speciation on the surfaces. Temperature programmed reduction (H_2-TPR) experiments (Fig. S1) confirmed the presence of reducible Fe_xO_y species (T_{max} ca. 400°C) in the Fe/Beta samples prepared by ion exchange and SMAD procedures. On the contrary, the high dispersed iron centers in Fe/ZSM-5 were characterized by very low reducibility (no peaks were detected in the 50-900°C temperature range). Because of the complex redox behavior of iron oxides, as previously studied by one of the authors,[54,55] it was not possible to give a quantitative insight into the stoichiometry of reduction of the Fe_xO_y species; the very different redox behavior of the iron species of the two zeolite structures, clearly evidenced from the reducing profiles, is the most distinctive feature of the samples.

The observed emerging different reducibility of iron species depending on zeolite structure/method of Fe-deposition provides the reasonable link between the nature of iron species in the catalysts and their catalytic behavior. Indeed, catalysts containing reducible Fe_xO_y aggregates were very active in the NH_3-SCO, while the low reducibility of isolated iron species in Fe/ZSM-5_{IE} is likely responsible for their inferior activity in the studied reaction.

3.3 Study of Used Catalysts

The high reproducibility observed over several runs on all the tested catalysts, suggested that the iron species introduced on zeolite framework are stable. To corroborate this evidence, the Beta zeolites after use were characterized by HAADF-STEM (Fig. 10). Both Fe/$Beta_{IE}$ and Fe/$Beta_{SMAD}$ *used* catalysts revealed the presence of FeO_x aggregates comparable in size respect to the corresponding *freshly* prepared samples. The results confirmed the high stability of the Beta zeolite-supported catalysts (both prepared by IE and SMAD) towards aggregation even when repeatedly subjected to temperatures up to 450°C, which was the highest operating temperature at which the catalytic tests were carried out.

4. CONCLUSIONS

Acetone solution containing solvated iron atoms was conveniently used to deposit Fe nanoparticles on Beta zeolite at low loading (Fe/BETA$_{SMAD}$, 2 wt. %), following the SMAD method. The combination of different characterization techniques (transmission electron microscopy, XPS and NH_3 adsorption experiments) revealed the presence of small FeO_x nanoparticles (d_m = 2.5 nm) highly dispersed on the Beta zeolite surface. The efficiency of the catalyst was evaluated in the selective catalytic oxidation of NH_3 to N_2 (NH_3-SCO), comparing its behavior with that obtained with catalysts prepared by classical IE method, containing the same Fe loading, and supported on Beta and ZSM-5 zeolite, respectively. All the catalysts exhibited high activity in the 300-450°C temperature range and remarkable selectivity towards N_2, when compared to an iron containing silica-alumina sample (Fe loading ca. 6 wt. %), used as reference material. Therefore, Fe/Beta$_{SMAD}$ was the best catalyst in terms of both activity (21.7 mmol g^{-1} min^{-1}) and selectivity to N_2 (> 99 % at 90 % conversion). Moreover, the catalyst exhibited a notable stability in reaction conditions even after four reaction runs.

ASSOCIATED CONTENT

The Supporting Information is available free of charge on the ACS Publications website at DOI: 10.xxx/acs.jpcc.xxxxxxxx.

■ AUTHOR INFORMATION

Corresponding Authors:

Antonella Gervasini, E-mail: antonella.gervasini@unimi.it
Dipartimento di Chimica, Università degli Studi di Milano, Italy
&
Claudio Evangelisti, E-mail: claudio.evangelisti@istm.cnr.it
CNR - ISTM - Istituto di Scienze e Tecnologie Molecolari, Italy

ORCID

Sebastiano Campisi: 0000-0002-5496-7482
Claudio Evangelisti: 0000-0002-8855-2592
Antonella Gervasini: 0000-0001-6525-7948

The authors declare no competing financial interest.

ASSOCIATED CONTENT

Supporting Information Available

The Supporting Information is available free of charge on the ACS Publications website at DOI: xxxxxxxx.

Assignment of UV-vis-DRS signals of Fe species on zeolites and H_2-TPR profiles of Fe-containing zeolites are reported.

ACKNOWLEDGMENTS

All the authors thank Ms. Iolanda Biraghi (from Università degli Studi di Milano, Dipartimento di Chimica) and Dr. Filippo Bossola (from CNR - ISTM - Istituto di Scienze e Tecnologie Molecolari), for performing some experimental analyses.

Pr. Stian Svelle, from University of Oslo (UiO), Norway, Chemistry Department, is gratefully acknowledged for providing zeolitic materials and Pr. Paolo Carniti from Università degli Studi di Milano, Dipartimento di Chimica, is acknowledged for the discussion on the reaction kinetic aspects.

REFERENCES

(1) International Fertilizer Industry Association *Global estimates of gaseous emissions of NH_3, NO and N_2O from agricultural land*. FAO: Rome, 2001.

(2) Backes, A. M.; Aulinger, A.; Bieser, J.; Matthias, V.; Quante, M. Ammonia Emissions in Europe, Part II: How Ammonia Emission Abatement Strategies Affect Secondary Aerosols. *Atmos. Environ.* **2016**, *126*, 153–161.

(3) Paulot, F.; Jacob, D. J.; Pinder, R. W.; Bash, J. O.; Travis, K.; Henze, D. K. Ammonia Emissions in the United States, European Union, and China Derived by High-Resolution Inversion of Ammonium Wet Deposition Data: Interpretation with a New Agricultural Emissions Inventory (MASAGE_NH3). *J. Geophys. Res.* **2014**, *119* (7), 4343–4364.

(4) Manahan, S. *Environmental Chemistry*, 10th Edition, CRC Press: New York, 2017.

(5) Erisman, J. W.; Schaap, M. The Need for Ammonia Abatement with Respect to Secondary PM Reductions in Europe. *Environ. Pollut.* **2004**, *129* (1), 159–163.

(6) European Environment Agency (EEA), Indicator Assessment: Ammonia (NH_3) emissions, 2015.

(7) Sapek, A. Ammonia Emissions from Non-Agricultural Sources. *Polish J. Environ. Stud.* **2013**, *22* (1), 63–70.

(8) Janssen, F. J. J. G.; Van Santen Rutger, A. *Environmental Catalysis Vol.1*; Imperial College Press: London, 1999.

(9) Busca*,* G.; Pistarino*,* C. Abatement of ammonia and amines from waste gases: a summary, *J. Loss Prev. Process Ind.* **2003***, 16*(2), 157–163.

(10) Chmielarz, L.; Jabłońska, M. Advances in Selective Catalytic Oxidation of Ammonia to Dinitrogen: A Review. *RSC Adv.* **2015**, *5* (54), 43408–43431.

(11) Offermans, W. K.; Jansen, A. P. J.; van Santen, R. A. Ammonia Activation on Platinum {111}: A Density Functional Theory Study. *Surf. Sci.* **2006**, *600* (9), 1714–1734.

(12) Ramis, G.; Yi, L.; Busca, G. Ammonia Activation over Catalysts for the Selective Catalytic Reduction of NO, and the Selective Catalytic Oxidation of NH_3. An FT-IR Study. *Catal. Today* **1996**, *28*, 373–380.

(13) Yuan, R. M.; Fu, G.; Xu, X.; Wan, H. L. Mechanisms for Selective Catalytic Oxidation of Ammonia over Vanadium Oxides. *J. Phys. Chem. C* **2011**, *115* (43), 21218–21229.

(14) Chen, W.; Qu, Z.; Huang, W.; Hu, X.; Yan, N. Novel Effect of SO_2 on Selective Catalytic Oxidation of Slip Ammonia from Coal-Fired Flue Gas over IrO_2 modified Ce-Zr Solid Solution and the Mechanism Investigation. *Fuel* **2016**, *166*, 179–187.

(15) Lenihan, S.; Curtin, T. The Selective Oxidation of Ammonia Using Copper-Based Catalysts: The Effects of Water. *Catal. Today* **2009**, *145* (1–2), 85–89.

(16) Il'chenko, N. I. Catalytic Oxidation of Ammonia. *Russ. Chem. Rev.* **1976**, *45* (12), 1119.

(17) Weststrate, C. J.; Bakker, J. W.; Gluhoi, A. C.; Ludwig, W.; Nieuwenhuys, B. E. Ammonia Oxidation on Ir(111): Why Ir Is More Selective to N2 than Pt. *Catal. Today* **2010**, *154* (1), 46–52.

(18) Lippits, M. J.; Gluhoi, A. C.; Nieuwenhuys, B. E. A Comparative Study of the Selective Oxidation of NH_3 to N_2 over Gold, Silver and Copper Catalysts and the Effect of Addition of Li_2O and CeOx. *Catal. Today* **2008**, *137* (2–4), 446–452.

(19) Schmidt-Szałowski, K.; Krawczyk, K.; Petryk, J. The Properties of Cobalt Oxide Catalyst for Ammonia Oxidation. *Appl. Catal. A* **1998**, *175* (1–2), 147–157.

(20) Ozkan, U. Role of Ammonia Oxidation in Selective Catalytic Reduction of Nitric Oxide over Vanadia Catalysts. *J. Catal*. 1993, pp 182–197.

(21) Hinokuma, S.; Shimanoe, H.; Kawabata, Y.; Kiritoshi, S.; Araki, K.; Machida, M. Supported and Unsupported Manganese Oxides for Catalytic Ammonia Combustion. *Catal. Commun.* **2018**, *105* (October 2017), 48–51.

(22) Chmielarz, L.; Kuśtrowski, P.; Rafalska-Łasocha, A.; Dziembaj, R. Selective Oxidation of Ammonia to Nitrogen on Transition Metal Containing Mixed Metal Oxides. *Appl. Catal. B Environ.* **2005**, *58* (3–4), 235–244.

(23) Lietti, L.; Ramis, G.; Busca, G.; Bregani, F.; Forzatti, P. Characterization and Reactivity of MoO_3/SiO_2 Catalysts in the Selective Catalytic Oxidation of Ammonia to N_2. *Catal. Today* **2000**, *61* (1–4), 187–195.

(24) Tang, X.; Li, J.; Yi, H.; Yu, Q.; Gao, F.; Zhang, R.; Li, C.; Chu, C. An Efficient Two-Step Method for NH_3 Removal at Low Temperature Using CoO_X -CuO_X /TiO_2 as SCO Catalyst Followed by $NiMn_2O_4$ as SCR Catalyst. *Energy & Fuels* **2017**, *31* (8), 8580–8593.

(25) Jabłońska, M.; Ciptonugroho, W.; Góra-Marek, K.; Al-Shaal, M. G.; Palkovits, R. Preparation, Characterization and Catalytic Performance of Ag-Modified Mesoporous TiO_2 in Low-Temperature Selective Ammonia Oxidation into Nitrogen and Water Vapour. *Microporous Mesoporous Mater.* **2017**, *245* (x), 31–44.

(26) Chmielarz, L.; Węgrzyn, A.; Wojciechowska, M.; Witkowski, S.; Michalik, M. Selective Catalytic Oxidation (SCO) of Ammonia to Nitrogen over Hydrotalcite Originated Mg-Cu-Fe Mixed Metal Oxides. *Catal. Letters* **2011**, *141* (9), 1345–1354.

(27) Long, R. Q.; Yang, R. T. Selective Catalytic Oxidation of Ammonia to Nitrogen over Fe_2O_3-TiO_2prepared with a Sol-Gel Method. *J. Catal.* **2002**, *207* (2), 158–165.

(28) Zhang, Q.; Wang, H.; Ning, P.; Song, Z.; Liu, X.; Duan, Y. In Situ DRIFTS Studies on CuO-Fe_2O_3catalysts for Low Temperature Selective Catalytic Oxidation of Ammonia to Nitrogen. *Appl. Surf. Sci.* **2017**, *419*, 733–743.

(29) Hung, C. M. Synthesis, Characterization and Performance of CuO/La_2O_3 composite Catalyst for Ammonia Catalytic Oxidation. *Powder Technol.* **2009**, *196* (1), 56–61.

(30) Jabłońska, M.; Wolkenar, B.; Beale, A. M.; Pischinger, S.; Palkovits, R. Comparison of Cu-Mg-Al-Ox and Cu/Al_2O_3 in Selective Catalytic Oxidation of Ammonia (NH_3-SCO). *Catal. Commun.* **2018**, *110*, 5–9.

(31) Jabłońska, M.; Palkovits, R. Copper Based Catalysts for the Selective Ammonia Oxidation into Nitrogen and Water Vapour-Recent Trends and Open Challenges. *Appl. Catal. B Environ.* **2016**, *181*, 332–351.

(32) Chmielarz, L.; Kuśtrowski, P.; Drozdek, M.; Dziembaj, R.; Cool, P.; Vansant, E. F. Selective Catalytic Oxidation of Ammonia into Nitrogen over PCH Modified with Copper and Iron Species. *Catal. Today* **2006**, *114* (2–3), 319–325.

(33) Akah, A.; Cundy, C.; Garforth, A. The Selective Catalytic Oxidation of NH_3 over Fe-ZSM-5. *Appl. Catal. B Environ.* **2005**, *59* (3–4), 221–226.

(34) Góra-Marek, K.; Brylewska, K.; Tarach, K. A.; Rutkowska, M.; Jabłońska, M.; Choi, M.; Chmielarz, L. IR Studies of Fe Modified ZSM-5 Zeolites of Diverse Mesopore Topologies in the Terms of Their Catalytic Performance in NH_3-SCR and NH_3-SCO Processes. *Appl. Catal. B Environ.* **2015**, *179*, 589–598.

(35) Qi, G.; Gatt, J. E.; Yang, R. T. Selective Catalytic Oxidation (SCO) of Ammonia to Nitrogen over Fe-Exchanged Zeolites Prepared by Sublimation of $FeCl_3$. *J. Catal.* **2004**, *226* (1), 120–128.

(36) Akah, A. C.; Nkeng, G.; Garforth, A. A. The Role of Al and Strong Acidity in the Selective Catalytic Oxidation of NH_3 over Fe-ZSM-5. *Appl. Catal. B Environ.* **2007**, *74* (1–2), 34–39.

(37) Qi, G.; Yang, R. T. Selective Catalytic Oxidation (SCO) of Ammonia to Nitrogen over Fe/ZSM-5 Catalysts. *Appl. Catal. A Gen.* **2005**, *287* (1), 25–33.

(38) Klabunde, K.J.; Li, Y.-X.; Tan, B.-J., Solvated Metal Atom Dispersed Catalysts, Chem. Mater. **1991**, *3*, 30-39.

(39) Evangelisti, C.; Schiavi, E.; Aronica, L. A.; Psaro, R.; Balerna A.; Martra, G. in Gold Catalysis: Preparation, Characterization and Applications, pp. 73-92, eds. L. Prati and A. Villa, CRC Press: New York, **2016**.

(40) Klabunde, K.; Sergeev, G., Nanochemistry 2°Ed., Elsevier, Amsterdam, **2013**.

(41) Oberhauser, W.; Evangelisti, C.; Jumde, R.P.; Petrucci, G.; Bartoli, M.; Frediani, M.; Mannini, M.; Capozzoli, L.; Passaglia, E.; Rosi, L. Palladium-nanoparticles on end-functionalized poly(lactic acid)-based stereocomplexes for the chemoselective cinnamaldehyde hydrogenation: Effect of the end-group, *J. Catal.* **2015**, *330*, 187–196.

(42) Oberhauser, W.; Evangelisti, C.; Tiozzo, C.; Vizza, F.; Psaro, R. Lactic Acid from Glycerol by Ethylene-Stabilized Platinum-Nanoparticles, *ACS Catalysis* **2016**, *6*, 1671-1674.

(43) Marelli, M.; Evangelisti, C.; Diamanti, M.V.; Dal Santo, V.; Pedeferri, M.P.; Bianchi, C.L.; Schiavi, L.; Strini, A. TiO2 Nanotubes Arrays Loaded with Ligand-Free Au Nanoparticles: Enhancement in Photocatalytic Activity, *ACS Appl. Mater. Interfaces*, **2016**, *8(45)*, pp 31051–31058.

(44) Marelli, M.; Jouve, A.; Villa, A.; Psaro, R.; Balerna, A.; Prati, L.; Evangelisti, C. Hybrid Au/CuO Nanoparticles: Effect of Structural Features for Selective Benzyl Alcohol Oxidation, J. Phys. Chem. C **2019,** DOI: 10.1021/acs.jpcc.8b09449.

(45) Jumde, R.P.; Evangelisti, C.; Mandoli, A.; Scotti, N.; Psaro, R. Aminopropyl-silica-supported Cu nanoparticles: An efficient catalyst for continuous-flow Huisgen azide-alkyne cycloaddition (CuAAC), *J. Catal.* **2015**, *324*, 25-31.

(46) Newsam, J. M.; Treacy, M.M.; Koetsier, W.T.; De Gruyter, C.B. Structural characterization of zeolite beta. *Proc. R. Soc. Lond. A* **1988**, *420*(1859), 375-405.

(47) Gervasini, A.; Marzo, M. Study of Influence of the Nature of the Support on the Properties of ferric oxide in relation to its activity in the decomposition of N_2O, *Ads. Sci. Technol.*, **2011**, *29*, 365-379.

(48) Barbaro, D.; Di Bari, L.; Gandin, V.; Evangelisti, C.; Vitulli, G.; Schiavi, E.; Marzano, C.; Ferretti, A.M.; Salvadori, P. Glucose-coated superparamagnetic iron oxide nanoparticles prepared by metal vapour synthesis are electively internalized in a pancreatic adenocarcinoma cell line expressing GLUT1 transporter, *Plos One* **2015**, *10*(4) 1-13.

(49) Cornell, R. M.; Schwertmann, U. Chapter 7 Characterization. In *The Iron Oxides*; Cornell, R. M., Schwertmann, U., Eds.; Wiley-VCH Verlag GmbH & Co. KGaA: Weinheim, FRG, 2003; pp 139–183.

(50) Gurgul, J.; Łątka, K.; Hnat, I.; Rynkowski, J.; Dzwigaj, S. Identification of Iron Species in FeSiBEA by DR UV-Vis, XPS and Mössbauer Spectroscopy: Influence of Fe Content. *Microporous Mesoporous Mater*. **2013**, *168*, 1–6.

(51) Kumar, M. S.; Schwidder, M.; Grünert, W.; Brückner, A. On the Nature of Different Iron Sites and Their Catalytic Role in Fe-ZSM-5 DeNOx Catalysts: New Insights by a Combined EPR and UV/VIS Spectroscopic Approach. *J. Catal.* **2004**, *227* (2), 384–397.

(52) Kumar, M. S.; Schwidder, M.; Grünert, W.; Bentrup, U.; Brückner, A. Selective reduction of NO with Fe-ZSM-5 catalysts of low Fe content: Part II. Assessing the function of different Fe sites by spectroscopic in situ studies, *J. Catal.* **2006**, *239*(1) 173-186.

(53) Brandenberger, S.; Kröcher, O.; Tissler, A.; Althoff, R. The determination of the activities of different iron species in Fe-ZSM-5 for SCR of NO by NH_3, *App. Catal. B* **2010**, *95*(3-4), 348-357.

(54) Gervasini, A.; Messi, C.; Carniti, P.; Ponti, A.; Ravasio, N.; Zaccheria, F. Insight into the Properties of Fe Oxide Present in High Concentrations on Mesoporous Silica. *J. Catal*. **2009**, *262* (2), 224–234.

(55) Messi, C.; Carniti, P.; Gervasini, A. Kinetics of Reduction of Supported Nanoparticles of Iron Oxide. *J. Therm. Anal. Calorim.* **2008**, *91* (1), 93–100.

Table 1 Morphological properties

Sample	Fe loading /wt.%	Specific Surface Area /m^2 g^{-1}	Micropore Volume /cm^3 g^{-1}
H-ZSM-5 [a]	-	413 (96%) [b]	0.165
H-Beta	-	418 (65%) [b]	0.121
Fe/ZSM-5$_{IE}$	1.7	385 (66%) [b]	0.117
Fe/Beta$_{IE}$	2.2	573 (42%) [b]	0.152
Fe/Beta$_{SMAD}$	2.0	367 (62%) [b]	0.101
Fe/SA	5.9	242	0.530

[a] obtained from NH_4-ZSM-5 after treatment at 550°C (5 h); [b] percent of internal surface area.

Table 2 Fe/zeolite catalyst properties

Sample	Fe loading /wt.%	Acidity [a] /μequiv g^{-1}	Surface Iron Concentration [b] /atom %	Mean Fe Particle Size /nm
Fe/ZSM-5_{IE}	1.7	1065.3	0.47	< LOD
Fe/$Beta_{IE}$	2.2	952.5	0.74	5.9 ± 1.8
Fe/$Beta_{SMAD}$	2.0	486.3	2.16	2.5 ± 0.7
Fe/SA	5.9	118.4	2.20	6.3 ± 3.0

[a] determined by NH_3 adsorption as reported in 2.3. paragraph (Catalyst Characterization); [b] determined by XPS analysis.

Table 3 Main catalytic results

Catalyst	Specific Activity [a] /μmol_{NH_3} g_{cat}^{-1} min^{-1}	Selectivity to N_2[b]/ %	Selectivity to NO_x [b]/ %	Selectivity to N_2O [b] / %	E_a / $kJ \cdot mol^{-1}$	ln A [c]
Fe/ZSM-5_{IE}	2200	98.83	0	1.17	100.0	21.35
Fe/$Beta_{IE}$	3600	98.74	0	1.26	97.5	21.72
Fe/$Beta_{SMAD}$	4900	99.54	0	0.46	140.0	30.14
Fe/SA	3200	92.70	0	7.30	133.2	28.47

[a] determined at 325°C (corresponding to NH_3 conversion in the range 4-18%); [b] evaluated at 90% of NH_3 conversion; [c] A, in $mmol_{NH_3}$ g^{-1} min^{-1}

Figures and Scheme

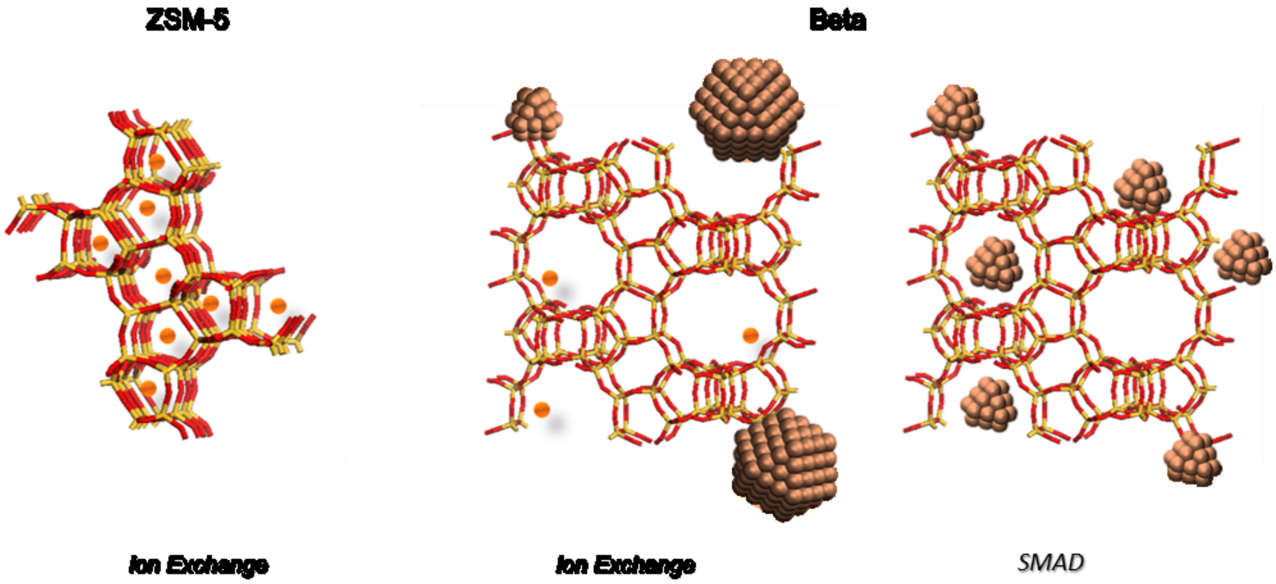

Scheme 1. Proposed iron nuclearity on ZSM-5 and Beta for IE and SMAD preparation methods.

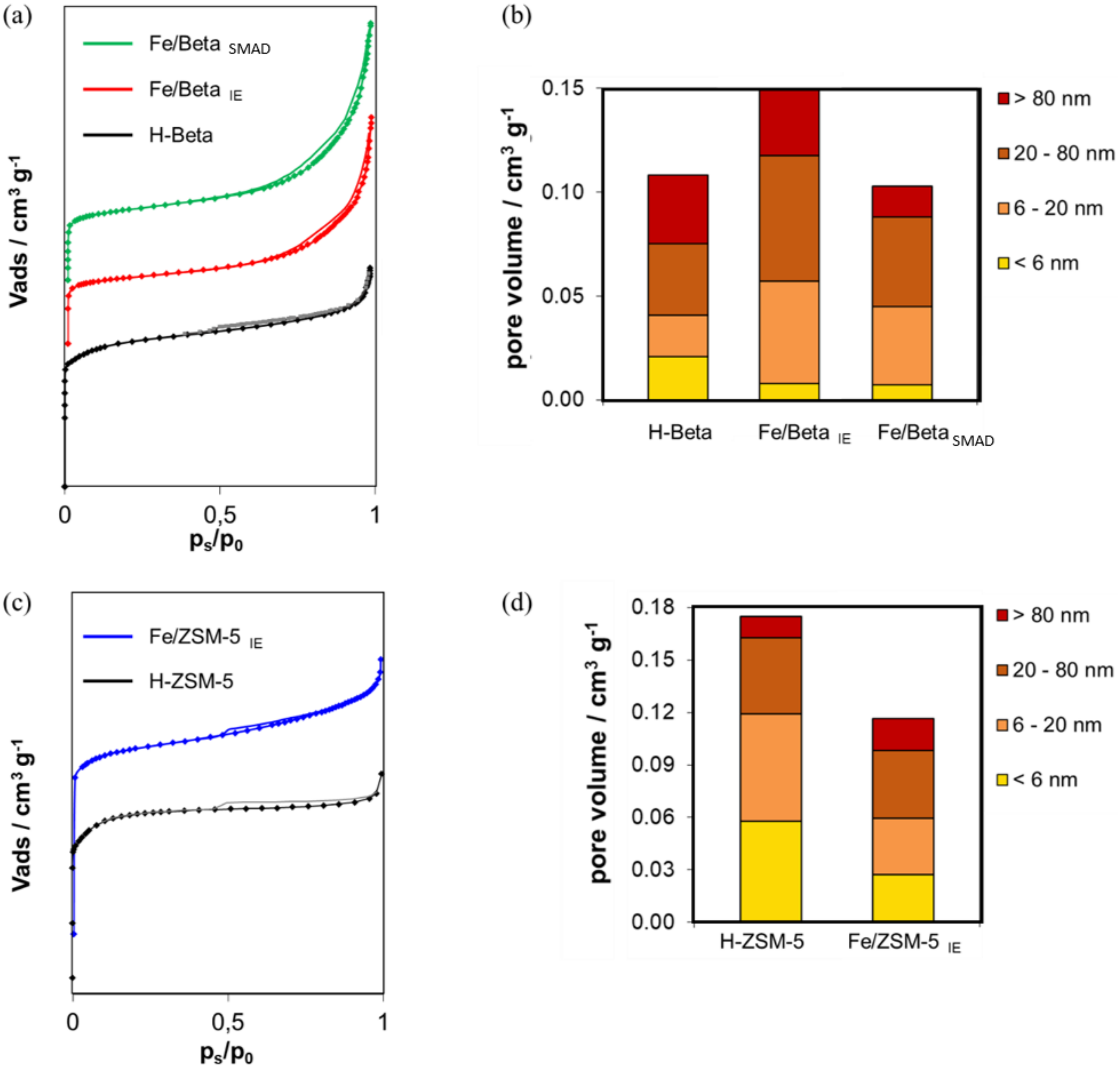

Figure 1. Results of the morphological properties determined by N_2 adsorption and desorption on bare and Fe-loaded zeolites: surface area and pore size distribution of Beta zeolite a) and b) and of ZSM-5 zeolite c) and d), respectively.

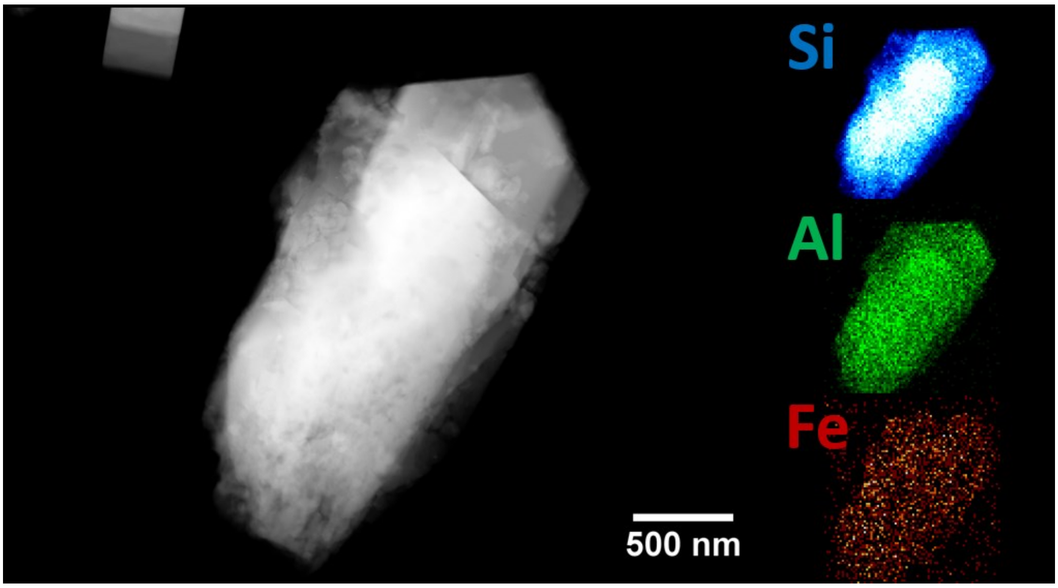

Figure 2. Representative STEM measurements of Fe/ZSM5$_{IE}$: HAADF image of a catalyst grain (left side); STEM-EDX element mapping (right side) of the catalyst showing the silicon (blue), aluminum (green) and Fe (red) maps.

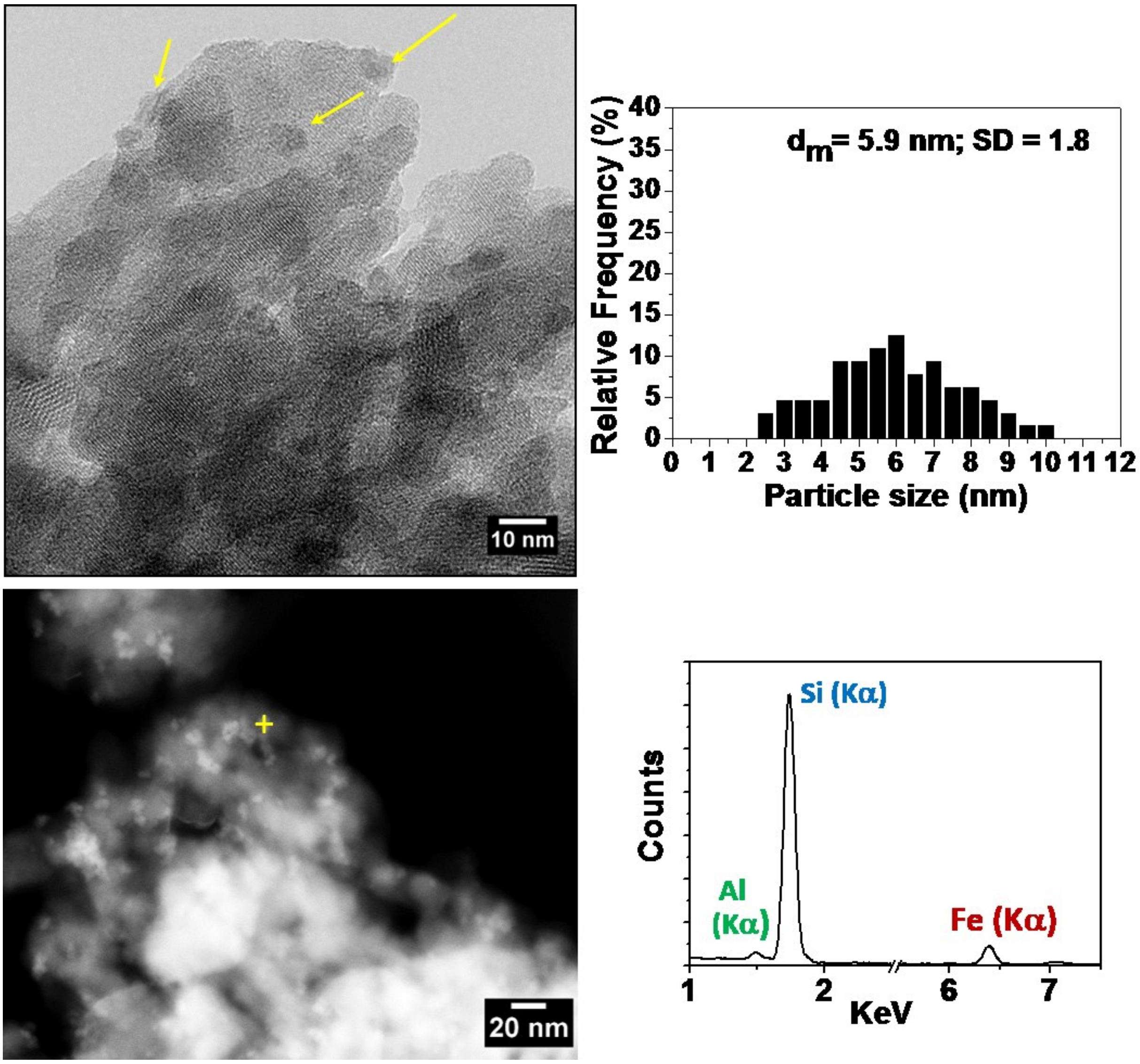

Figure 3. Representative HR-TEM and related histogram of particle size distribution of $\text{Fe/Beta}_{\text{IE}}$ (top). HAADF-STEM micrograph and EDX spectrum of the selected spots of $\text{Fe/Beta}_{\text{IE}}$ (bottom).

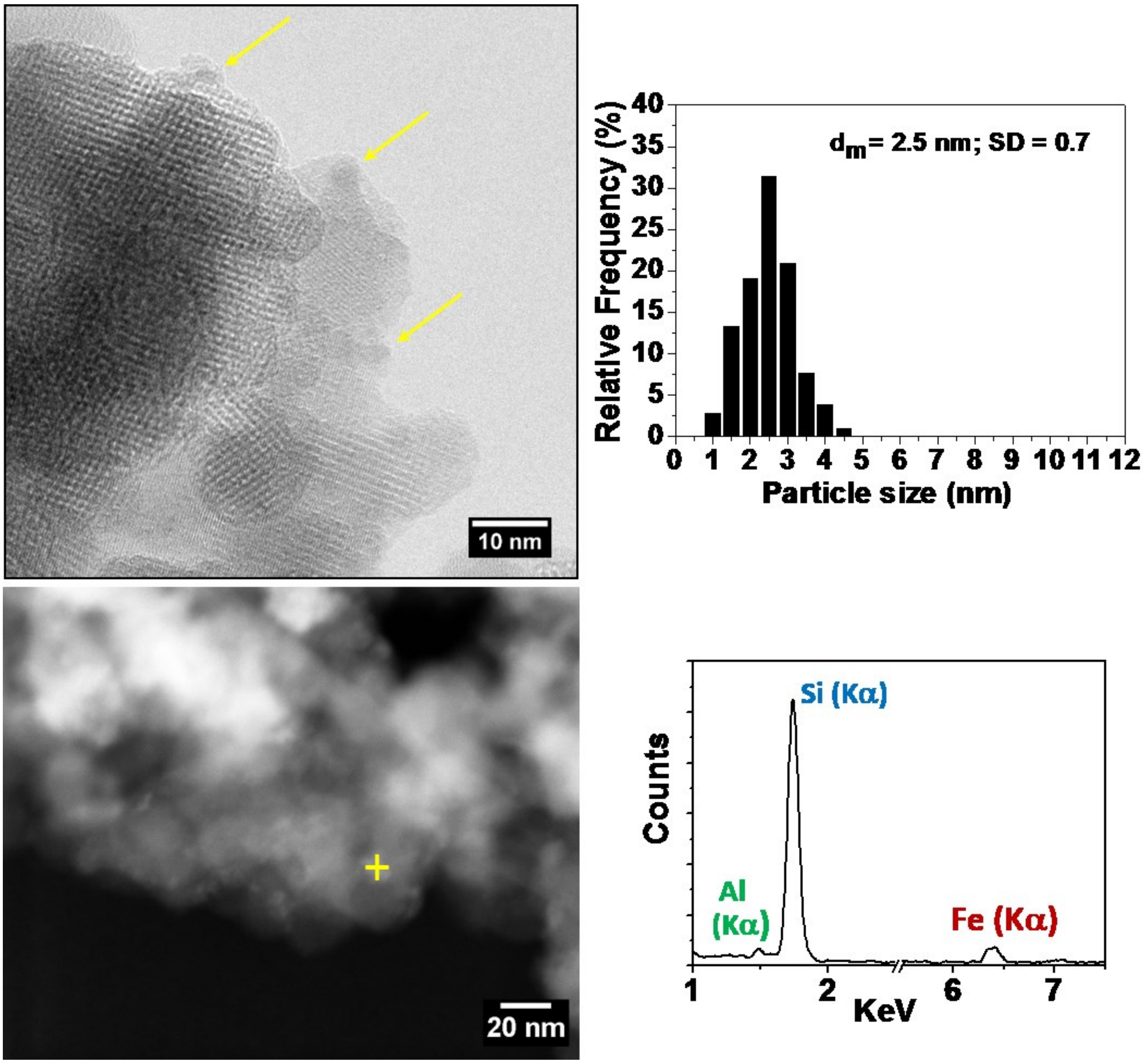

Figure 4. Representative HR-TEM and related histogram of particle size distribution of Fe/Beta$_{\mathrm{SMAD}}$ (top). HAADF-STEM micrograph and EDX spectrum of the selected spots of Fe/Beta$_{\mathrm{SMAD}}$ (bottom).

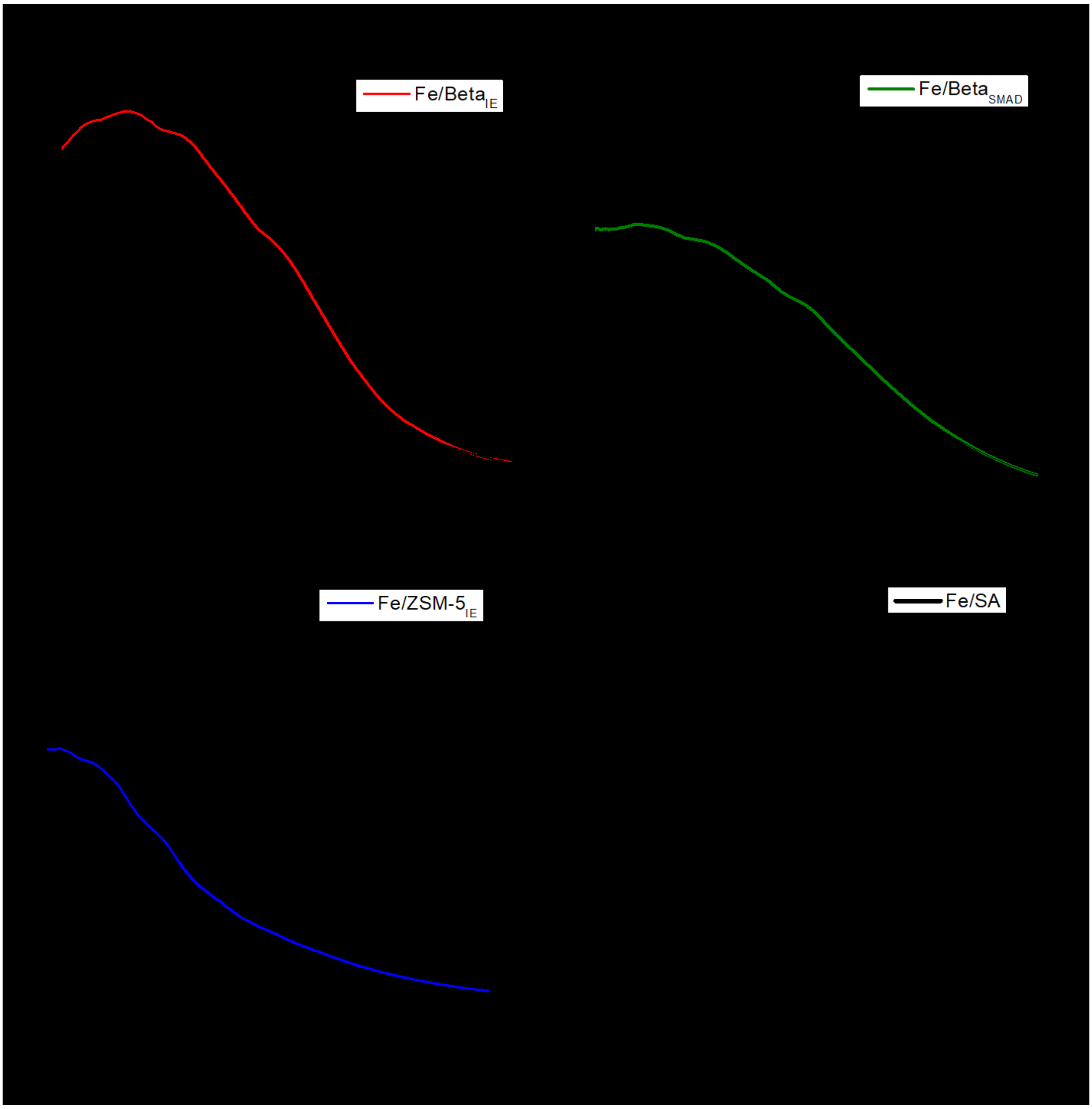

Figure 5. UV-vis-DR spectra of the Fe-zeolites. Colored curves correspond to experimental spectra and black curves to calculated sub-bands; sum of the sub-bands give the calculated spectra overlapping the experimental ones.

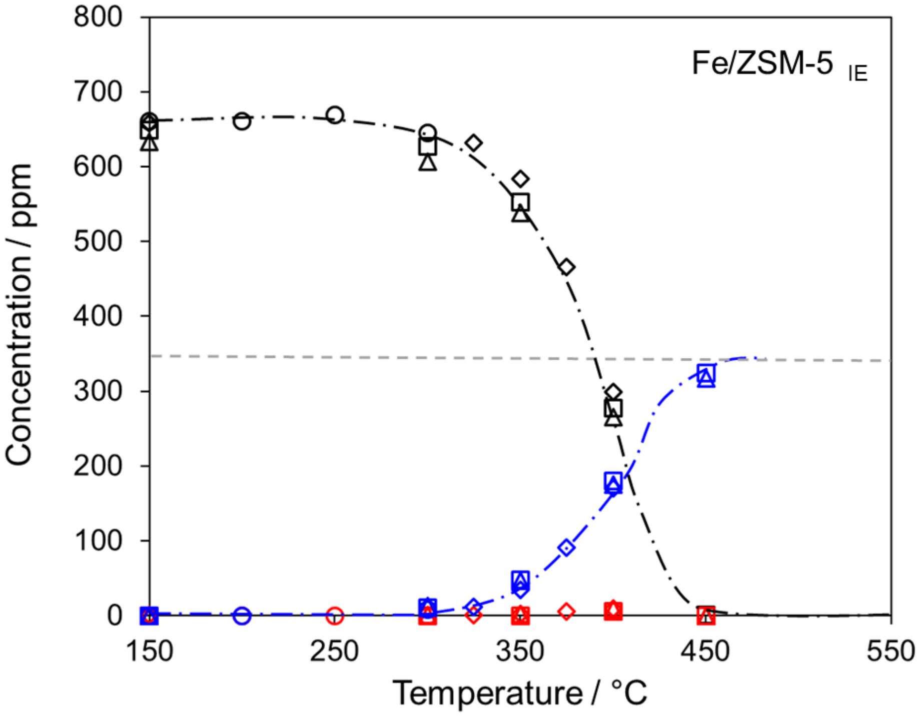

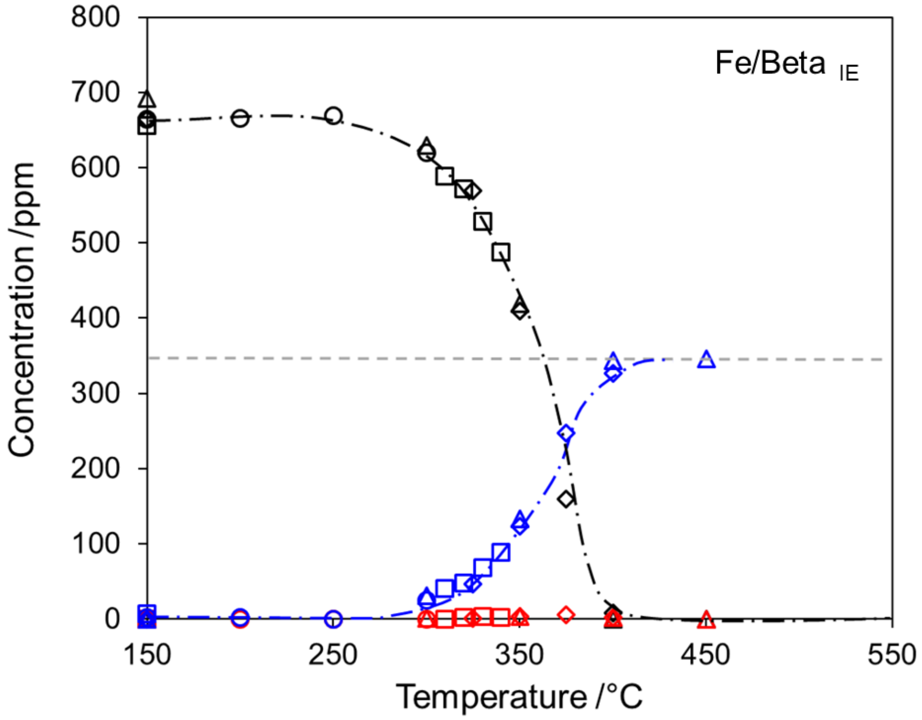

Figure 6. Concentration profiles of NH_3 (black markers), N_2 (blue markers), and N_2O (red markers) as a function of reaction temperature in the ammonia selective catalytic oxidation reaction on Fe/ZSM-5$_{IE}$ (top) and Fe/Beta$_{IE}$ (bottom). Different symbols correspond to different catalytic runs.

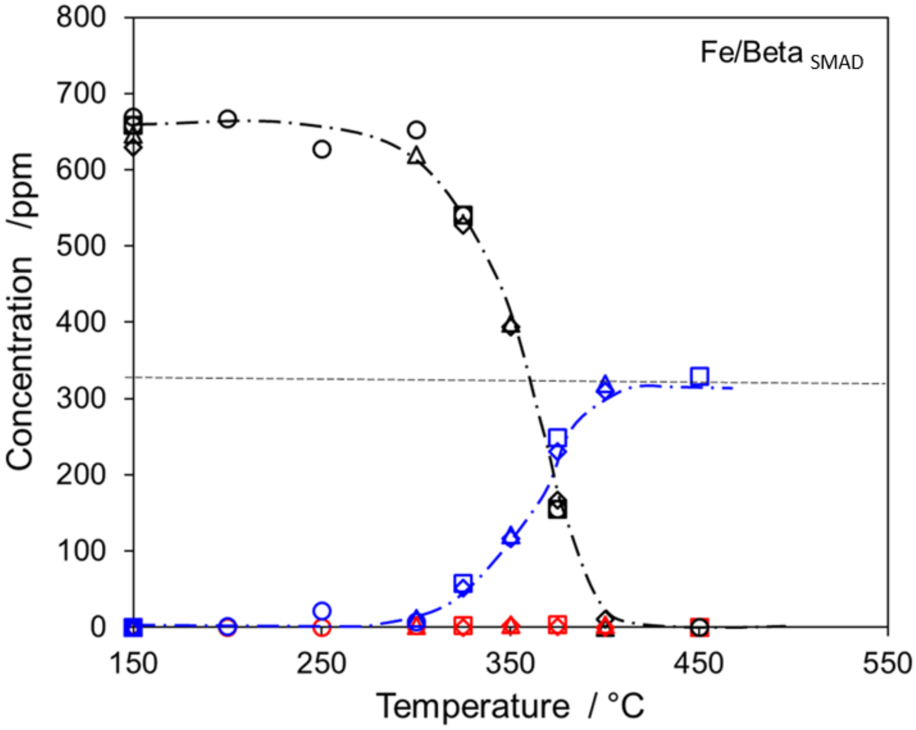

Figure 7. Concentration profiles of NH_3 (black markers), N_2 (blue markers), and N_2O (red markers) as a function of reaction temperature in the ammonia selective catalytic oxidation reaction on Fe/Beta$_{SMAD}$. Different symbols correspond to different catalytic runs.

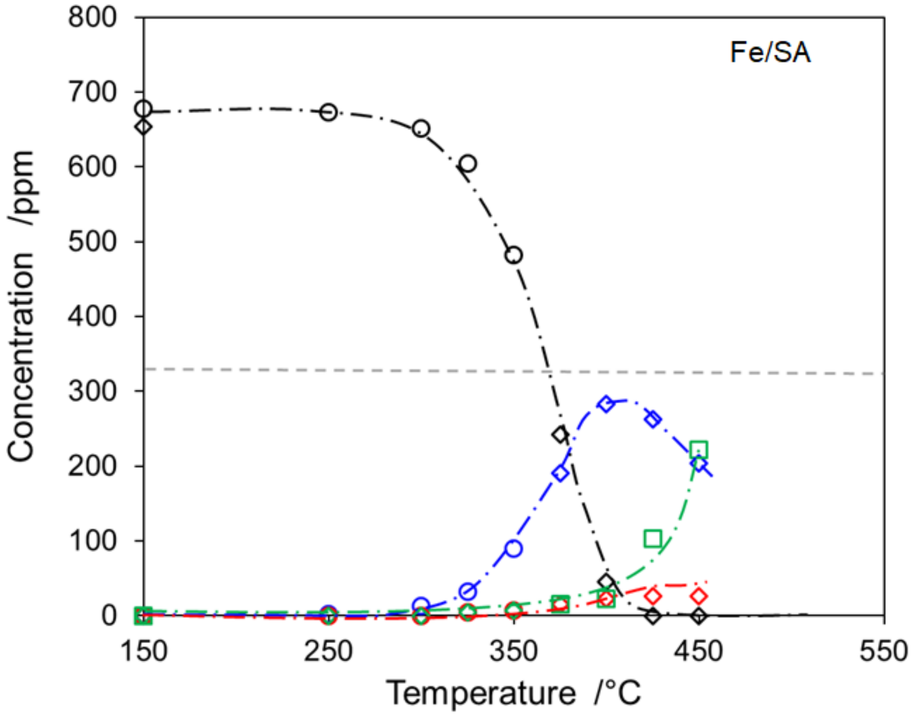

Figure 8. Concentration profiles of NH_3 (black markers), N_2 (blue markers), N_2O (red markers), and NO (green markers) as a function of reaction temperature in the ammonia selective catalytic oxidation reaction on Fe/SA. Different symbols correspond to different catalytic runs.

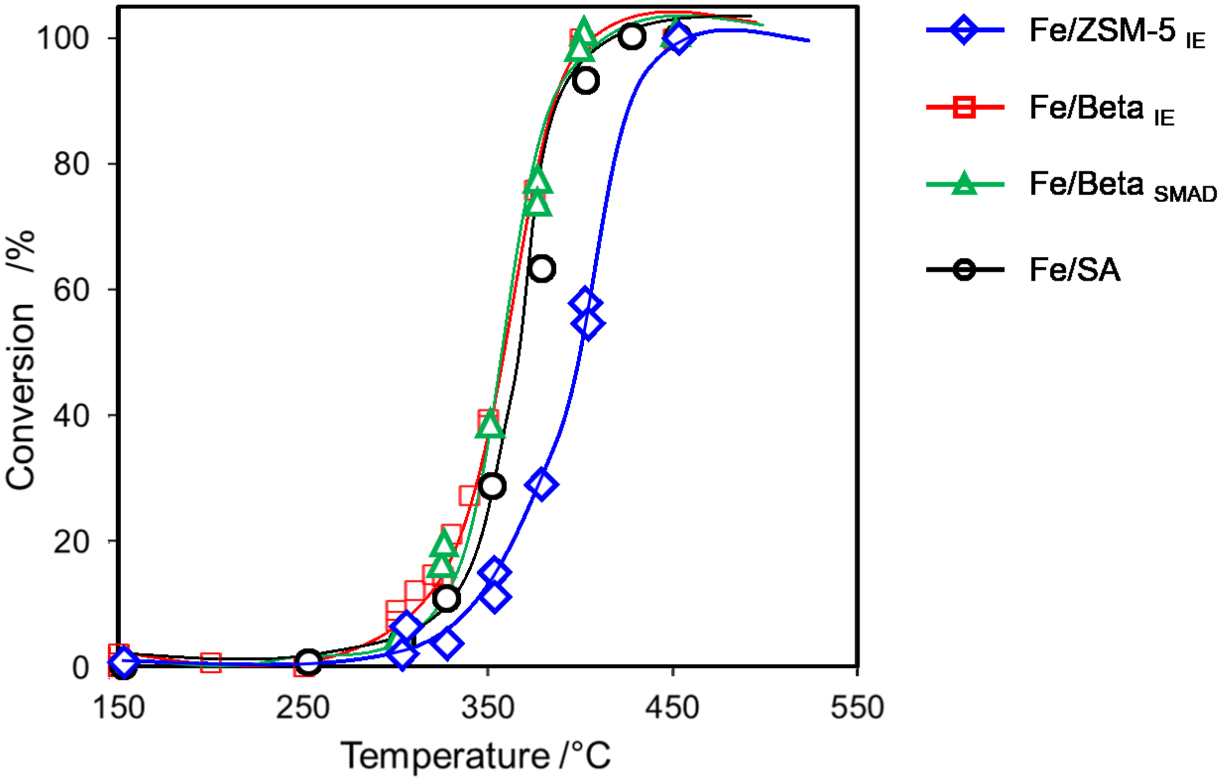

Figure 9. Comparative curves of ammonia conversion as a function of reaction temperature on the studied iron based zeolites.

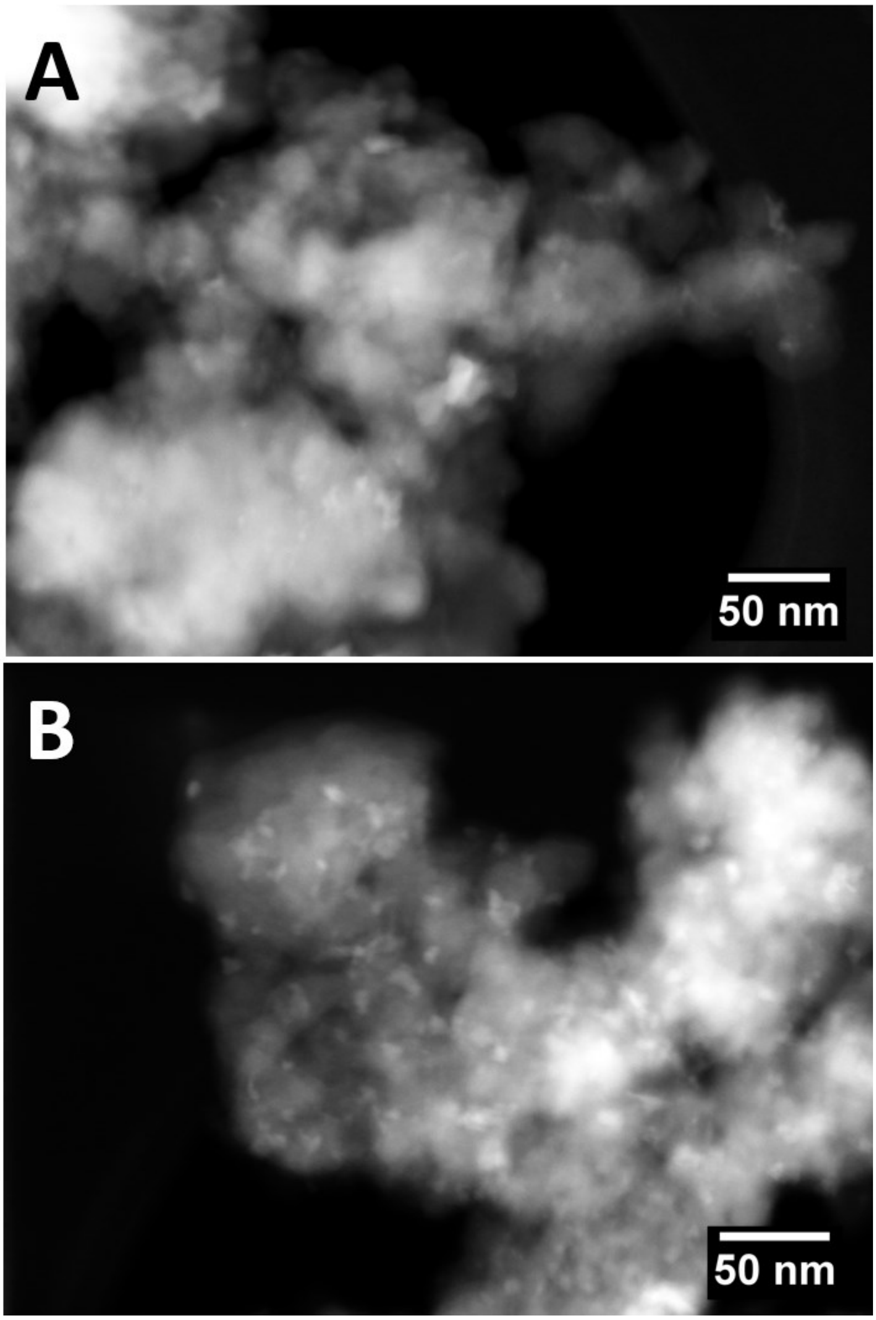

Figure 10. Representative HAADF-STEM micrograph of *used* Fe/Beta$_{\mathrm{SMAD}}$ (A) and *used* Fe/Beta$_{\mathrm{IE}}$ (B).

TOC graphic

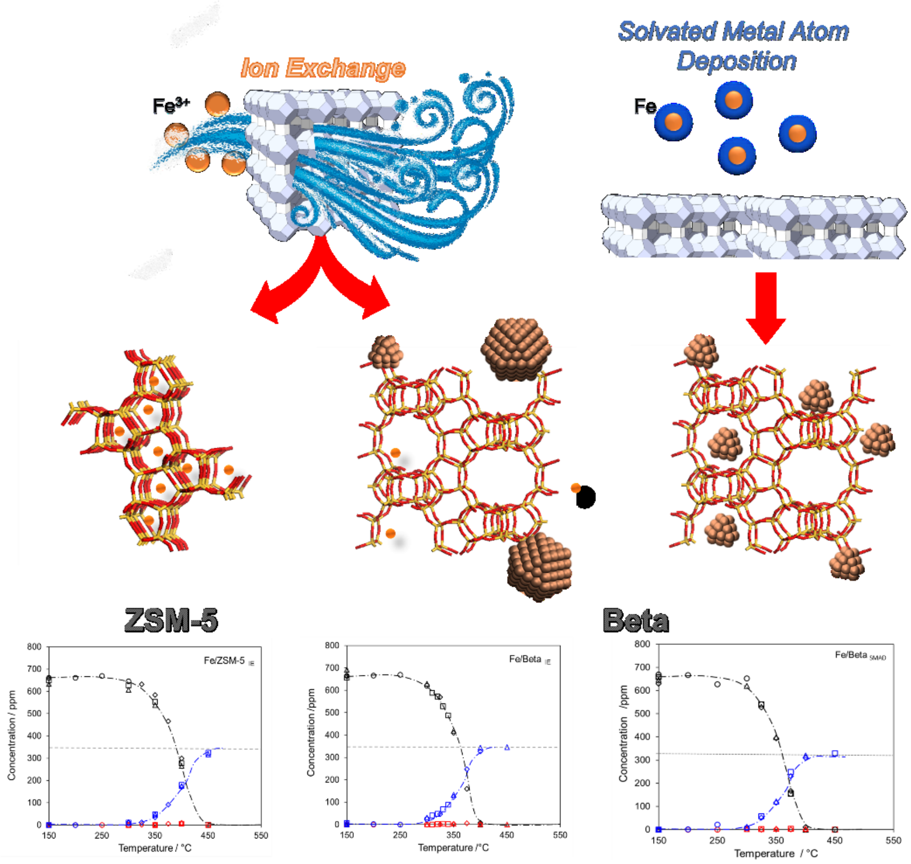
Ion Exchange
Fe3+
Solvated Metal Atom Deposition
Fe
ZSM-5
Beta
Fe/ZSM-5 IE
Fe/Beta IE
Fe/Beta SMAD
Concentration / ppm
Temperature / °C
0
100
200
300
400
500
600
700
800
150
250
350
450
550